Advances in Geo-Energy Research

Vol. 17, No. 3, p. 184-195, 2025

Original article

Integrated detection of micro-pore structures and macro-mechanical responses for hydrate-bearing sediments

Yajuan Zhang[1,2], Yunkai Ji[2], Minhui Qi[1], Lin Dong[1], Sunhao Zhang[3], Yanlong Li[1]*

[1]*Laoshan Laboratory, Qingdao 266237, P. R. China*

[2]*Key Laboratory of Gas Hydrate, Ministry of Natural Resources, Qingdao Institute of Marine Geology, Qingdao 266237, P. R. China*

[3]*Graduate School of Engineering, Nagasaki University, Nagasaki 8528521, Japan*

Keywords:
Hydrate-bearing sediment
transverse relaxation time
magnetic resonance imaging
pore structure
failure mechanism

Cited as:
Zhang, Y., Ji, Y., Qi, M., Dong, L., Zhang, S., Li, Y. Integrated detection of micro-pore structures and macro-mechanical responses for hydrate-bearing sediments. Advances in Geo-Energy Research, 2025, 17(3): 184-195.
https://doi.org/10.46690/ager.2025.09.02

Abstract:
Micro-pore structures determine the macro-mechanical behaviors of porous media, whereas their quantitative linkages remain ambiguous owing to the limitations of test techniques, especially for hydrate-bearing sediments. This study proposes an integrated approach that combines low-field nuclear magnetic resonance high-frequency detection with triaxial shearing, enabling the *in-situ* simultaneous monitoring of both the macro-mechanical parameters and micro-pore structures. The device, which consists of a high-pressure specimen vessel, a low-field nuclear magnetic resonance measurement module, a temperature and pressure control module, and a data acquisition module, allows the real-time acquisition of transverse relaxation time distribution and magnetic resonance images during triaxial loading, facilitating the detection of pore water distribution and crack development. Preliminary verification illustrates the high reliability of the device. Under relatively low strain, the signal intensity ratio of micropores rises with a transverse relaxation time of less than 10 ms, while that of macropores decreases gradually. Conversely, the signal intensity ratios for both micropores and macropores present the opposite tendency with the strain exceeding 5.1%. Besides, with the axial strain rising from 0 to 15%, there is an increase of about 16.9% in the peak area of macropores. Randomly distributed cracks observed under triaxial shearing correspond to the increasing peak area and signal intensity ratio of macropores, which is verified by comparing the magnetic resonance and computerized tomography images. This method provides a new possibility for characterizing the failure processes of hydrate-bearing sediments and establishing macro-to-micro equivalent relationships, enhancing the applications for porous media containing phase-reversible agents.

1. Introduction

Natural gas hydrates (NGH) are widely accepted as one of the most promising alternative energy sources of the 21st century (Makogon et al., 2007; Walsh et al., 2009). During their exploitation process, large-scale NGH dissociation will inevitably weaken the cementation effect, generate excess pore pressure, and alter reservoir stability (Sloan, 2003). In addition, various engineering and geo-mechanical challenges may arise, such as wellbore instability, drilling platform overturning, and submarine landslides (Hyodo et al., 2017; Li et al., 2021a; Zhang et al., 2024a). The stability evaluation of hydrate reservoirs is a prerequisite for safe and sustainable production (Hyodo et al., 2012). Therefore, investigating the evolution law of the mechanical properties of hydrate-bearing sediments (HBS) has great theoretical significance and engineering application value in enhancing the production

Yandy Scientific Press

*Corresponding author.
E-mail address: zhangyjhhu@163.com (Y. Zhang); jiyunkai@yeah.net (Y. Ji); mhqi@qnlm.ac (M. Qi); donglinupc@163.com (L. Dong); 17854262633@163.com (S. Zhang); ylli@qnlm.ac (Y. Li).

Received July 2, 2025; revised July 27, 2025; accepted August 16, 2025; available online August 21, 2025.

efficiency and ensure safe exploitation.

The macroscopic mechanical response of HBS corresponds to the microstructural changes and local damage during the shear process (Dong et al., 2024; Zhang et al., 2024b). Specifically, micro-pore structures exhibit continuous changes in shape and distribution under loading, which mainly reflects the macro-mechanical behaviors and damage degree of HBS (Li et al., 2021b; Sohn et al., 2024). Conversely, changes in the microstructure, such as crack propagation and the formation of shear bands, can affect the strength and deformation characteristics (Miyazaki et al., 2012). In this regard, understanding the microstructural changes of HBS is crucial for analyzing its shear failure mechanisms (Yoneda et al., 2019). However, due to the limitations of current test technologies, research on the microscopic deformation and failure mechanism of HBS remains inadequate.

Low-field nuclear magnetic resonance (LF-NMR) technology has been applied to characterize the distribution and content of pore water (Minagawa et al., 2012). Dynamic changes in the pore structure during hydrate formation can be sensitively detected by LF-NMR, which is manifested by the shift of transverse relaxation time distribution range and peak value (Shumskayte et al., 2021). Typically, decreasing pore size and increasing pore specific surface area will shorten the transverse relaxation time (T_2), accompanied by a leftward shift of the peak (Bukhanov et al., 2022). In contrast, the increase in pore size and the formation of microcracks will cause a rightward shift of the peak or the emergence of a new peak (Kossel et al., 2018). However, traditional LF-NMR detection is unfavorable for the real-time detection of microstructural damage corresponding to macro-mechanical behaviors.

Currently, the LF-NMR assisted triaxial shearing test is frequently used to study the microscopic damage evolution of geotechnical materials, including rock, coal and clay (Zhao et al., 2022; Bi et al., 2023). For example, Bi et al. (2023) investigated the evolution patterns of micropores, mesopores and macropores in sandstone during the shear process and revealed the rock damage mechanisms based on the variation in real-time T_2 and magnetic resonance imaging (MRI). Zhao et al. (2022) studied the dynamic evolution of pore structure and fracture development of coal specimens under different stress states by synchronous analysis of real-time T_2 spectra and MRI. Subsequently, Zhou et al. (2022) presented a comprehensive quantitative characterization and visualization of pores and cracks in coal by MRI-assited triaxial shearing tests. However, these coupling techniques are not suitable for HBS because they cannot achieve the simultaneous monitoring of mechanical parameters and NMR signals under specific pressure and temperature conditions. Therefore, there is an urgent need to develop a novel triaxial shear test system with LF-NMR real-time measurement for HBS, enabling the precise detection of the coupling mechanisms between macro-mechanical responses and micro-structural evolution.

This study introduces a novel device and experimental methodology that integrates LF-NMR with the triaxial shear test for HBS. Detailed components of the device, experimental procedures, and data processing methods will be successively presented. To date, this is the first time to realize the real-time LF-NMR *in-situ* detection during the triaxial shearing of HBS specimens. In addition, preliminary experimental results will be provided to demonstrate the usability, flexibility and reliability of the technique. This method provides a new approach for exploring the interconnectedness of macro-micro damage in HBS under loading.

2. Device development

2.1 General description

The diagram of LF-NMR and the triaxial shear real-time online system is shown in Fig. 1. The system is primarily composed of a high-pressure specimen vessel, an LF-NMR measurement module, a temperature and pressure control module, and a data acquisition module. The high-pressure vessel enables artificial HBS synthesis and axial loading, enabling immediate *in-situ* triaxial shearing after specimen preparation. The LF-NMR measurement module is responsible for specimen preservation, as well as T_2 spectrum and MRI measurement. The temperature and pressure control module provides high-pressure methane gas for hydrate synthesis, pumps Pre-cooled Fluorinert liquid (3M) to supply a targeted confining pressure for the specimen, and keeps a relatively low temperature, which is crucial for the thermal stability of hydrates in the specimen. The data acquisition module records all data obtained from the LF-NMR measurement module and the temperature and pressure control module, and it is also responsible for driving the axial loading module.

2.2 High-pressure specimen vessel

The high-pressure specimen vessel is used for specimen preparation and axial loading applications. As seen in Fig. 2, the vessel consists of a load cylinder, an axial metal guide rod, a top seal cover, two polyetheretherketone (PEEK) rods, a joint lever, and a heat-shrinkable tube. The HBS specimen is installed inside the heat-shrinkable tube and its two ends are tightly confined by the PEEK rods. The heat-shrinkable tube and the PEEK rods are sealed with sealing rings. In the middle of the PEEK rods, a gas pipe is designed, enabling high-pressure gas injection at both ends to form hydrates. The dimension of the HBS specimen is Φ25 mm × H50 mm. To ensure the sustainability of the experiment, it is necessary to configure a safety valve for this module and adjust its safety pressure to 18 MPa.

Moreover, to aid axial loading for the high-pressure specimen vessel, a constant-flux pump, a constant-flux pump water tank, and a safety valve are fitted. The maximum axial loading force is 5 kN, the maximum axial displacement is 25 mm, and the axial loading rate is adjustable within the range of $0 \sim 5$ mm/min. To enable real-time monitoring, an axial stress sensor and a displacement sensor are installed at the top and end of the high-pressure vessel.

2.3 LF-NMR measurement module

The LF-NMR measurement module is used to detect the ^{1}H signal inside the specimen. It consists of an LF-NMR

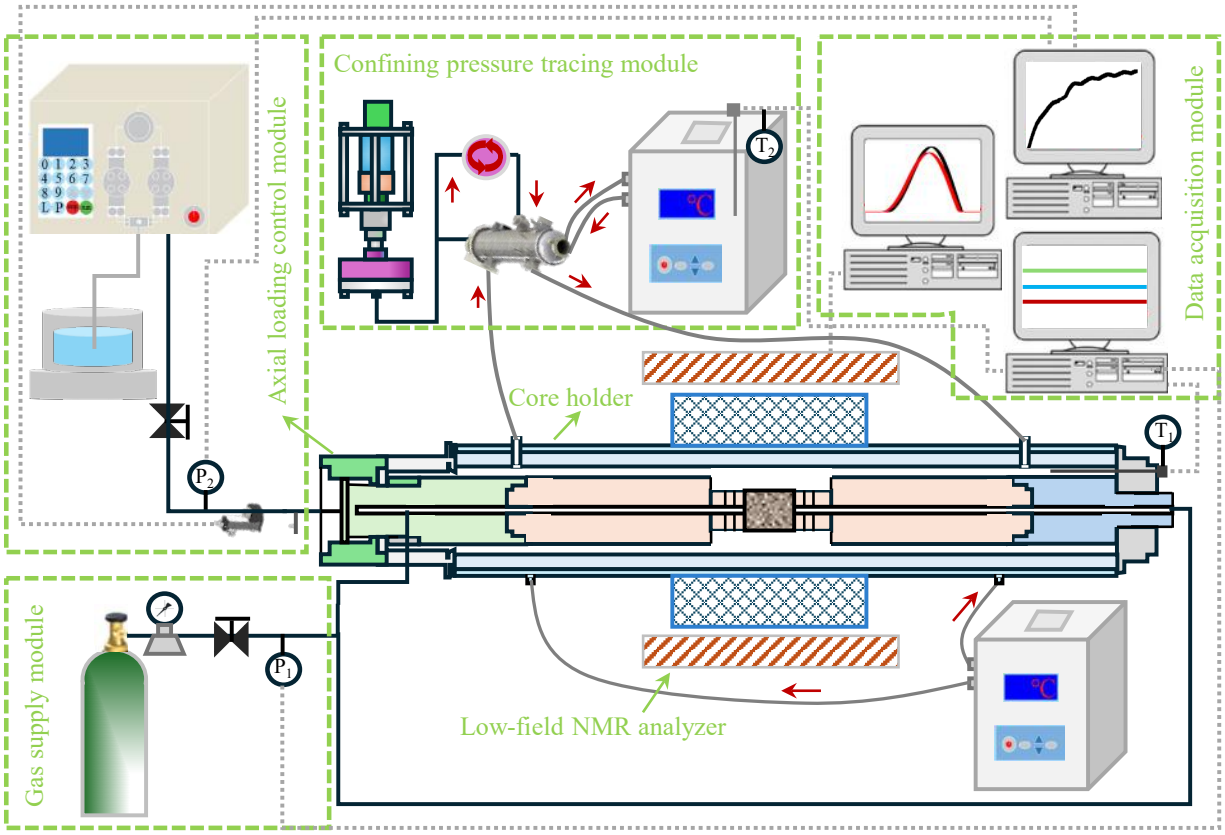

Fig. 1. Schematic diagram of the LF-NMR and triaxial shear real-time online system.

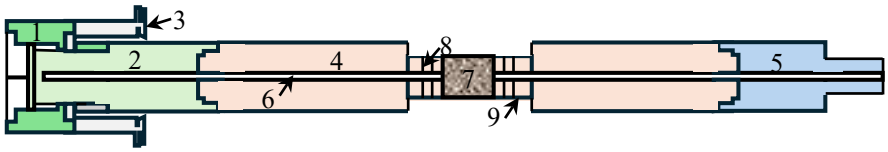

Fig. 2. The schematic diagram of high-pressure specimen vessel (1-load cylinder; 2-axial guiding rod; 3-top seal cover; 4-PEEK rod; 5-joint lever; 6-gas pipe; 7-HBS specimen; 8-sealing ring; 9-heat-shrinkable tube).

analyzer (MesoMR23-060H, Suzhou Niumag Analytical Instrument Co., Ltd.) and a core holder. This module can obtain real-time T_2 spectra and MRI during hydrate formation and HBS specimen shearing. The LF-NMR analyzer is composed of a spectrometer control unit, a NdFeB permanent magnet, a temperature control unit, a radio frequency unit, and a gradient unit. The working temperature of the NdFeB permanent magnet is maintained at 32 ± 0.1 °C by the temperature control unit. The NdFeB permanent magnet can produce a uniform magnetic field of 20 ppm with 60 mm in length. The magnetic field intensity is about 0.5 T. The ^{1}H Larmor frequency is 21.3 MHz. Imaging gradients in the X, Y and Z directions can be independently amplified using the gradient unit, with a peak gradient strength of 5 Gauss/cm.

The core holder consists of a confining pressure fluid outlet, inner ring cavity, radiofrequency coil, confining pressure fluid inlet, outer ring fluid inlet, outer ring cavity, and outer ring fluid outlet, as shown in Fig. 3(a). Its shell is mainly made of PEEK, and the raw material of the heat-shrinkable tube is fluorinated ethylene propylene. These two materials have no effect on the magnetic field and radiofrequency field. A multi-layer composite thermal insulation structure is applied between the inner and outer ring cavities. The inner layer (cold source side) and the outer layer (contact constant temperature side) are sleeves made of non-magnetic material PEEK. Furthermore, the gap between the inner and outer layers is evacuated to eliminate thermal convection and heat conduction. The diameter of the radiofrequency coil is 70 mm. During the experiment, the high-pressure specimen vessel should be placed in the inner ring cavity of the core holder. The front sealing cover, core holder and back sealing cover are connected by the threaded connection and rubber ring seal. The high-pressure specimen vessel is sealed with the inner ring cavity of the core holder to form a confining pressure chamber. The stress state of the specimen is shown in Fig. 3(b). The circulating fluid (Fluorinert liquid, 3M) in the outer ring cavity should be kept constant at 32 °C to avoid affecting the magnet temperature. During the experiment, T_2 spectrum and MRI of

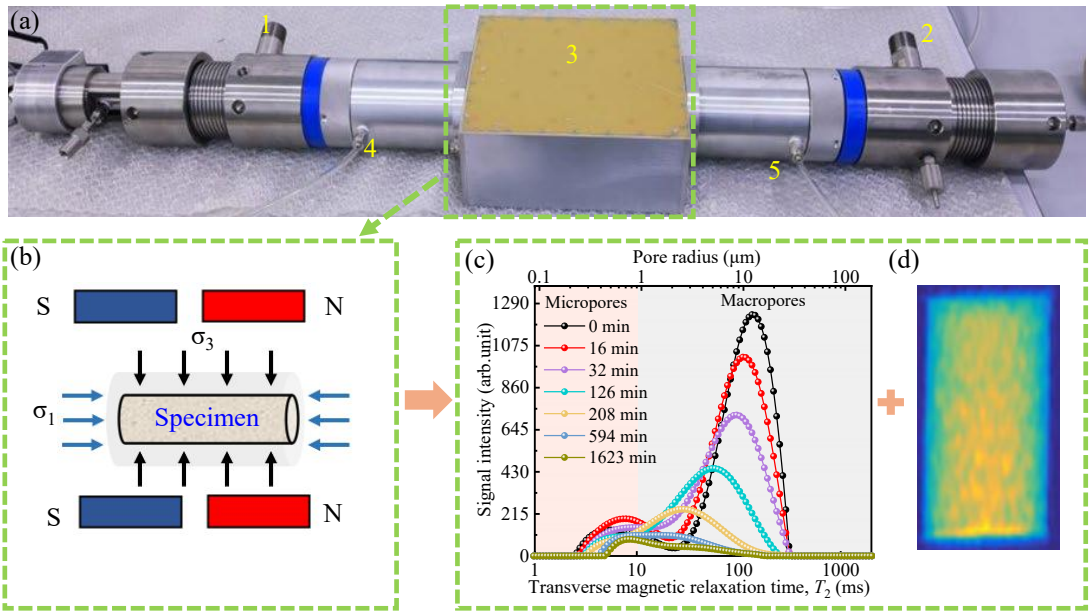

Fig. 3. Structure of the core holder. (a) Physical picture, (b) stress state of the specimen under loading, (c) T_2 distribution and (d) MRI (1-confining pressure fluid outlet; 2-confining pressure fluid inlet; 3-radiofrequency coil; 4-outer ring fluid outlet; 5-outer ring fluid inlet).

HBS specimens are collected in real time, as shown in Figs. 3(c)-3(d).

2.4 Temperature and pressure control module

The temperature and pressure control module can maintain the specimen temperature, effective confining pressure, and sediment pore pressure at the target value to facilitate the control of hydrate formation and HBS shear operations. This module includes a gas supply unit, a temperature control unit, and a confining pressure tracking unit. The gas supply unit consists of a high-pressure gas cylinder, a pressure reduction valve, a back-pressure valve, a pressure sensor, and gas pipelines. In the experiments, gas is injected simultaneously into both ends of the specimen to accelerate hydrate formation.

The confining pressure tracking unit enables the dual control of temperature and confining pressure, comprising a Fluorinert liquid storage tank, a confining pressure tracking pump, a cryogenic bath, a closed-cycle cryostat, a circulating pump, and circulation pipelines. The Fluorinert liquid (FC-40, 3M) without the NMR signal is used as a confining pressure fluid and temperature control fluid, and its low dielectric property can minimize radio-frequency loss (Ersland et al., 2010). Fluorinert liquid is pumped into the circulation pipeline via the confining pressure tracking pump. After being cooled by the cryogenic bath, it enters the circulating pump to maintain a constant temperature for the specimen. The confining pressure tracking pump can keep the effective confining pressure of the specimen constant to prevent the heat-shrinkable tube from bursting. The closed-cycle cryostat is designed to maintain the circulation of Fluorinert liquid in the outer ring cavity of the core holder, thereby avoiding low-temperature Fluorinert liquid in the inner ring cavity from impacting the permanent magnet temperature.

2.5 Data acquisition module

The data acquisition module consists of temperature sensors, pressure sensors, an axial displacement sensor, an axial stress sensor, and computers. The locations of the temperature and pressure sensors are shown in Fig. 1. Temperature sensor T_1 directly monitors the temperature of Fluorinert liquid circulating in the inner ring cavity. Since the liquid is in direct contact with the specimen, T_1 provides an accurate representation of the specimen temperature, while T_2 measures the cooling bath temperature. Pressure sensor P_1 is positioned at the outlet of the gas cylinder and the front end of the gas inlet line to monitor gas pressure, and P_2 is located at the front end of the axial loading piston for the real-time measurement of axial stress. Pressure sensors with a measurement accuracy of ±0.15% are used to measure pore pressure and confining pressure. PT100 temperature sensors, with an accuracy of ±0.1 °C, monitor the temperatures of Fluorinert liquid and the low-temperature bath. The shear deformation of the specimen is measured by an axial displacement transducer with a high accuracy of ±0.01 mm. Finally, the T_2 distribution and MRI of the specimen are acquired using an LF-NMR analyzer.

3. Test methods

The experimental workflow comprises four sequential stages, as illustrated in Fig. 4, including specimen preparation, specimen synthesis, HBS triaxial shear test with LF-NMR online monitoring, and CT-based verification. Stage three captures the time-dimensional damage evolution data during shearing, focusing on revealing the dynamic damage mechanisms. Stage four can be used to reconstruct the 3D

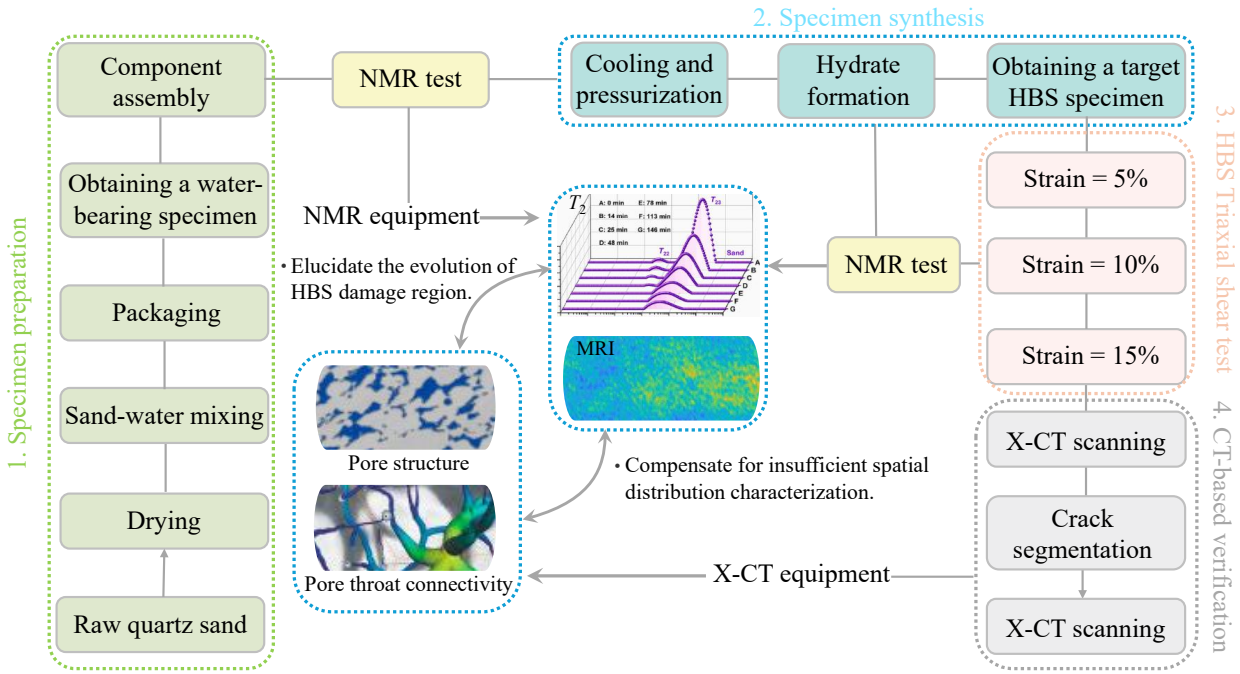

Fig. 4. The experimental workflow diagram.

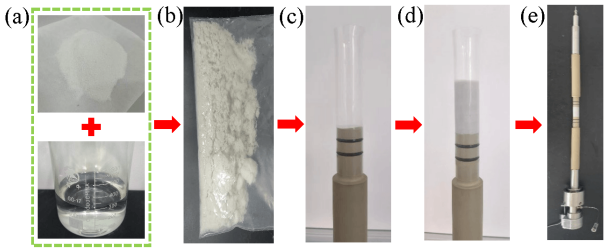

Fig. 5. Sampling steps for the water-bearing sediments. (a) Sediments and deionized water, (b) water-bearing sediments, (c) the heat-shrinkable tube adheres to the sidewall of the PEEK, (d) sampling and (e) well-assembled high-pressure vessel.

fracture networks of the post-failure HBS specimen, emphasizing the verification of damage evolution conclusions from the spatial dimension. Stages three and four complement each other and are both indispensable.

3.1 Specimen preparation

First, deionized water and a gas source are provided. The target sediment is placed in a dryer and kept at 120 °C until its mass becomes constant (see Fig. 5(a)). An appropriate amount of sediment and deionized water are weighed and mixed evenly to configure water-bearing sediments (see Fig. 5(b)). Next, the 125 mm heat-shrinkable tubing is cut, and one end of about 40 mm length is sleeved at the end of the PEEK top rod. This is followed by treatment with a hot-air blower to make it shrink and tightly adhere to the sidewall of the PEEK top bar, yielding a final size of the heat-shrinkable tube at Φ25 mm × H120 mm. Afterwards, a filter paper is placed at the bottom of the heat-shrinkable tube to prevent sediments from blocking the gas pipe of the PEEK top rod (see Fig. 5(c)). Next, the water-bearing sediments are divided into five equal parts and then filled into the heat-shrinkable tube and compacted in layers. After the first four layers have been compacted, the upper surface of sediments is scraped to avoid delamination, thus obtaining a water-bearing sediment specimen with dimensions of Φ25 mm × H50 mm (see Fig. 5(d)). A filter paper is placed on the upper surface of the specimen and each component is assembled (see Fig. 5(e)). Finally, the assembly Fig. 5(e) is installed into the core holder, and the end caps and pipelines are securely connected to ensure sealing integrity. Each module and its corresponding pipelines are connected.

3.2 NGH synthesis

1) The closed-cycle cryostat is filled with fluorinated liquid. The closed-cycle cryostat for the outer ring cavity is activated and set to the magnet operating temperature (32 °C), followed by circulation for at least 30 minutes to stabilize the magnetic environment. Subsequently, the cryogenic bath for the inner ring cavity is initiated and set to 2 °C with circulation enabled. The cover of the fluorinated liquid storage tank is opened and the tank is filled until the fluorinated liquid level stabilizes. The cover is then securely fastened. The circulation pump is started at a speed of 1,000 rpm/min to ensure fluorinated liquid circulation. A confining pressure of 2.5 MPa is set and maintained by the tracking pump. The storage tank is kept open to discharge air and then closed. The supply bottle is periodically refilled to provide enough fluorinated liquid during the whole process. The target confining pressure is realized once the effective confining pressure reaches 2.5 MPa.
2) The temperature-pressure data are collected. Once the

confining pressure is up to the target value, the T_2 distribution and MRI of the specimen are tested. Next, the methane gas cylinder and inlet valve are kept open to allow the pore pressure to increase. The pressure reducer valve is adjusted to stabilize the pore pressure at 6 MPa, upon which the hydrate formation experiment is commenced. To avoid interference with magnetic signals, the effective confining pressure, pore pressure and temperature are kept constant during hydrate formation. Hydrate formation is considered to be over when the deionized water consumption rate becomes less than 1×10^{-5} g/h. During this process, the T_2 distribution and MRI of the specimen are collected.

3) To obtain more high-quality MRI in subsequent triaxial shear tests, the pore pressure inlet valve is closed and the pore pressure outlet valve is opened after hydrate formation. When the pore pressure is lower than the phase equilibrium pressure, the pore pressure outlet valve is closed to decompose part of the hydrates. Hydrate dissociation will lead to a gradual increase in pore pressure. After the pore pressure rises to the phase equilibrium pressure, hydrates will no longer decompose. In this process, the T_2 distribution of specimens should be continuously monitored.
4) The real-time liquid water content in the specimen can be calculated by the T_2 distributions. Step 3) is repeated to decompose the hydrates until a clear MRI is obtained. At this time, a constant amount of liquid water is maintained, the HBS specimen synthesis is completed, and the T_2 distribution and MRI in this state are detected.

3.3 Joint test

1) The tank is filled with water and connected with a constant-flux pump before axial loading. The initial axial displacement is set to 0 mm, and then the specimen is compressed at a shear rate of 0.2 mm/min. The test data is monitored and recorded through control software during the shear process, while the T_2 spectrum and MRI are collected continuously.
2) Due to the long time consumed by MRI, the shear process is divided into three shear stages of 0-5%, 5%-10% and 10%-15%, as shown in Fig. 6, to obtain shear details of the specimen as much as possible. The MRI and T_2 spectra are acquired before and after each shear stage. The triaxial shear test is considered to be over when the shear strain reaches 15%.

3.4 Data processing

Based on the test principles of LF-NMR, the T_2 of pore fluids in porous media involves three independent mechanisms: Volume relaxation, surface relaxation, and diffusion relaxation. However, in a sediment system with small pores and coexisting gas-water phases, both volume relaxation and diffusion relaxation can be neglected (Slijkerman et al., 2001). Therefore, T_2 is calculated as follows:

$$T_2 = \frac{V_p}{\rho_2 S_p} \tag{1}$$

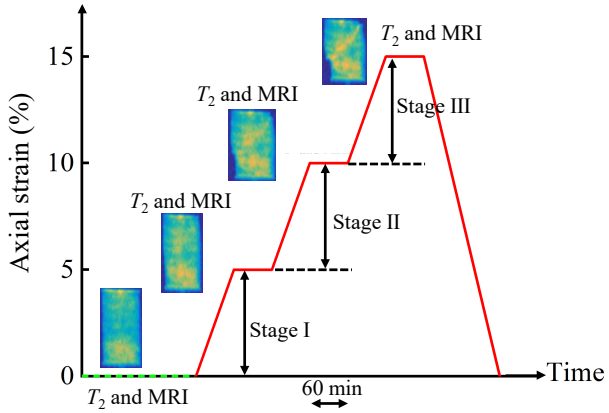

Fig. 6. Experimental procedures for LF-NMR and triaxial shear online joint test.

where V_p/S_p represents the ratio of pore volume to surface area. It is known that the pore can be regarded as spherical, $V_p/S_p = r/3$; r represents the pore radius; ρ_2 represents the transverse surface relaxation rate of porous media. The quartz sand ρ_2 used in this study is 30 μm/s (Liu et al., 2021), so T_2 is proportional to r.

Studies have shown that the cumulative amplitude of T_2 distribution is an effective method to determine the liquid water content in sediment pores (Ji et al., 2022; Wang et al., 2024). All T_2 distributions of LF-NMR standard samples with different water contents are obtained at 2 °C. A calibration equation that can be used to calculate the water contents of water-bearing sediments is derived by linearly fitting the water contents and cumulative amplitudes of T_2 distribution about standard samples:

$$m_w = kI \tag{2}$$

where m_w represents the water content of the specimen, g; I represents the cumulative amplitudes of T_2 distribution of the specimen, arb.unit; k represents the uncertainty coefficient, g. In this paper, k is equal to 2.1841×10^4.

The apparent volume of the specimen is:

$$V_c = \frac{\pi D^2 L}{4} \tag{3}$$

where V_c represents the apparent volume of the specimen, mm^3; D and L are respectively the diameter and length of the specimen, mm. In this paper, D and L are 25 and 50 mm, respectively.

The water saturation of the specimen is calculated as:

$$S_w = \frac{m_w}{\rho_w V_p} \times 100\% = \frac{m_w}{\rho_w V_c \varphi} \times 100\% \tag{4}$$

where ρ_w represents the density of deionized water, 1.0 g/cm^3; V_p represents the pore volume of the sediments, cm^3; φ represents the porosity of the sediments, %.

The volume of methane gas is proportional to its signal cumulative amplitude. The expression is:

$$V_g = aI_g \tag{5}$$

where V_g represents the volume of methane gas, cm^3; I_g represents the signal cumulative amplitude of methane gas, arb.unit;

a is the uncertainty coefficient. In this verification experiment, the initial methane gas volume of the water-bearing sand specimen is $V_{g0} = V_p - V_{w0} = 9.82 - 5.96 = 3.86$ cm^3, where V_{w0} represents the initial water volume, cm^3. When the pore pressure increases from atmospheric pressure up to 6 MPa, the cumulative amplitude of the T_2 spectrum signal rises from 25,660.16 arb.unit to 27,365.47 arb.unit. Thus, the obtained uncertainty coefficient is $a = 3.86/(27365.47 - 25660.16) = 2.263\,52 \times 10^{-3}$.

Combining Eqs. (2) and (5), the water content of the specimen during hydrate formation is shown as:

$$m_w = k\left(I - \frac{V_g}{a}\right) \tag{6}$$

Based on the molecular structure of methane hydrate $CH_4 \cdot 6H_2O$ (Sloan et al., 2008), the hydrate volume and hydrate saturation of the specimen can be determined as shown in Eqs. (7) and (8), respectively.

$$V_h = \frac{m_h}{\rho_h} = \frac{\frac{(m_{w0} - m_w)}{18 \times 6}(16 + 18 \times 6)}{\rho_h} \tag{7}$$

$$S_h = \frac{V_h}{V_c \varphi} \tag{8}$$

where V_h represents the methane hydrate volume, cm^3; m_h represents the methane hydrate mass, g; ρ_h represents the density of methane hydrate, 0.914 g/cm^3 (Wu et al., 2018); and m_{w0} is the initial water content of the specimen, g; S_h represents hydrate saturation, %.

The volume of methane gas in the specimen, V_g, is calculated as follows:

$$V_g = V_p - V_w - V_h \tag{9}$$

where V_w represents water volume, cm^3.

The axial stress σ_a during the triaxial shear loading of the HBS specimen is calculated as follows:

$$\sigma_a = \frac{A_l \sigma_p - A_t \sigma_c}{A_s} = \frac{907.92\sigma_p - 417.05\sigma_c}{490.87} \tag{10}$$

where σ_a represents the axial stress, MPa; σ_p represents the axial compressive force, MPa; σ_c represents the confining pressure, MPa; A_l represents the piston area of the loading cylinder, $A_l = \pi r_l^2 = \pi \times 17^2$ mm^2 = 907.92 mm^2; A_s represents the cross-sectional area of the specimen, $A_s = \pi r_s^2 = \pi \times 12.5^2$ mm^2 = 490.87 mm^2; At represents the circumferential area of the metal adapter, $A_t = \pi(r_l^2 - r_t^2) = \pi \times (17^2 - 12.5^2)$ mm^2 = 417.05 mm^2.

3.5 CT-based verification

Since some pores in the aforementioned HBS specimens are not filled with water, their T_2 distributions can only partially reflect the specimen's pore structure characteristics. X-CT scanning is performed on the failed specimen to deepen insights into the crack development characteristics and verify the damage evolution conclusions of HBS. Each X-CT scanning takes about 22 minutes, producing 1,000-slice images with a resolution of 6 μm. Subsequently, Avizo software is employed for crack segmentation. The procedures include:

1) Removing the background noise;
2) Performing global threshold segmentation on the grayscale core images;
3) Extracting the pore structure;
4) Applying watershed algorithms to segment interconnected pores or particles.

Finally, the continuous distribution of large-scale pore structure is determined as cracks based on the pore volume statistical distribution characteristics.

4. Verification experiments and results

4.1 Materials and procedures

Sediment used for the verification experiment was purchased from Shanghai Bofei Meike Chemical Technology Co., Ltd. To remove impurities prior to use, the sediment underwent pretreatment steps, including drying and cleaning, then it was screened to ensure that the particle size distribution was in the range of 120-180 mesh. The grain size distribution curve of quartz sand is shown in Fig. 7(a). After analysis and testing, the particle size distribution of quartz sand was between 34 ~ 373 μm, with a median particle size (d_{50}) of 143.56 μm. The dry density (ρ_s) of the sediment was 2.65 g/cm^3. Methane gas (99.99%, Qingdao Dehai Weiye Technology Co., Ltd.) and deionized water were used to synthesize methane hydrates.

First, 39.02 g sand and 6.12 g deionized water were weighed to prepare water-bearing sand with a porosity (φ) of 0.40 and an initial water saturation (S_{w0}) of 60.74%. Next, the packing of water-bearing sand and module assembly were completed in strict accordance with Section 3.1. Fig. 7(b) presents the temperature and pressure path diagram of experiments. Hydrates were generated by the excess gas method. During hydrate formation, the low-temperature bath was maintained at 2 °C, and the pore pressure and effective confining pressure were kept at 6.0 and 2.5 MPa (see Fig. 8(a)), respectively. When hydrates were no longer generated, the effective confining pressure was adjusted to 1.5 MPa. Next, the pore pressure was reduced to 3 MPa, so that some hydrates could decompose. This operation was repeated until the water content in the specimen reached 1.8 g. Subsequently, the specimen was kept stable concerning 3.78 MPa pore pressure (the phase equilibrium pressure for CH_4 hydrate at 2 °C, see Fig. 8(b)). Joint tests of LF-NMR and triaxial shear on HBS specimens were performed with the shear rate of 0.2 mm/min.

4.2 Verification of the device via hydrate formation experiment

At first, the hydrate formation experiment was carried out, and the experimental data were compared with the previous ones to prove the reliability and accuracy of the equipment, so as to lay the foundation for subsequent research. Referring to the pore classification of coal, shale and quartz sand (Yao et al., 2010; Zhou et al., 2022), $T_2 \leq 10$ ms and $T_2 > 10$ ms are considered micropores and macropores, respectively. In addition, the micropore/macropore ratio refers to the specific value of microporous/macroporous signal intensity to the total signal intensity in T_2 distributions.

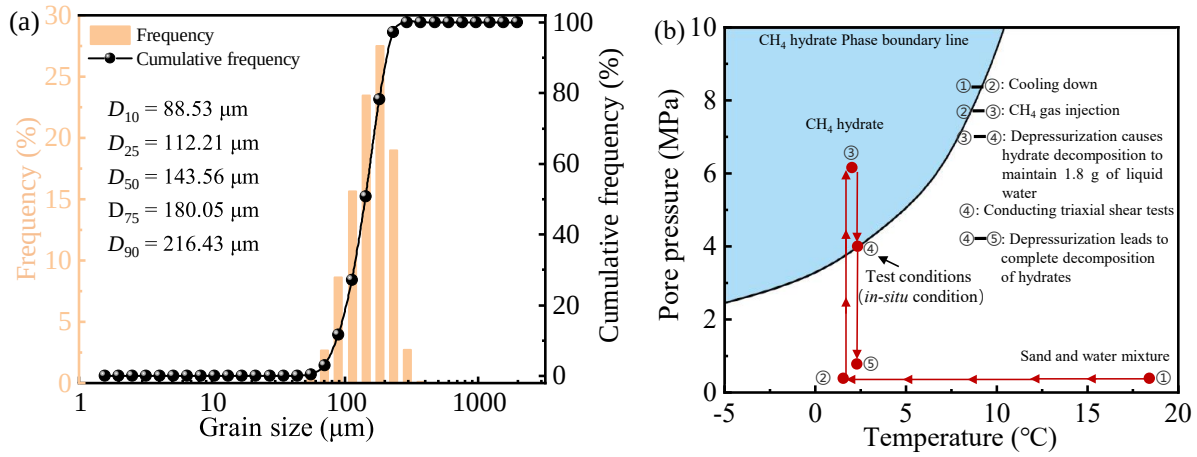

Fig. 7. (a) Particle size distribution curve of quartz sand and (b) temperature and pressure path diagram of experiments.

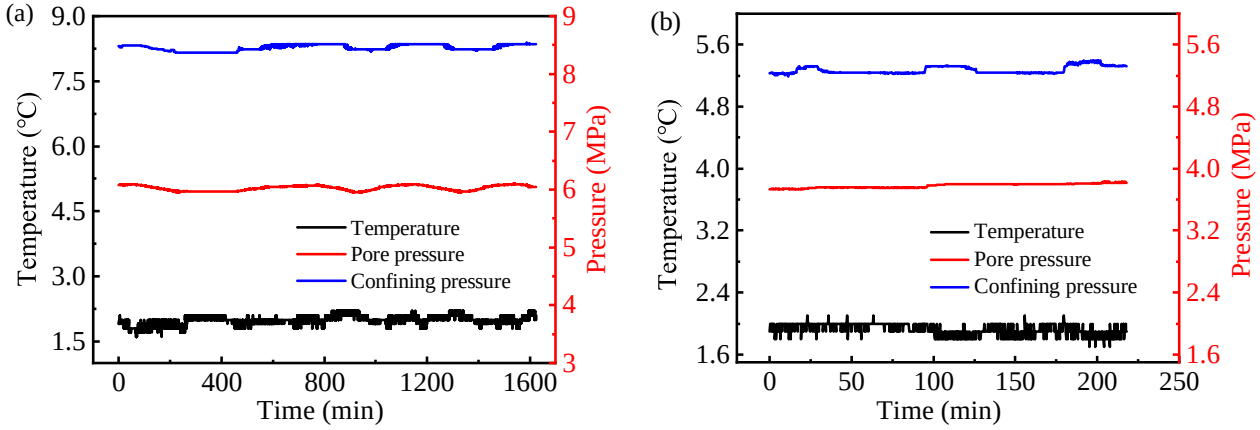

Fig. 8. Variation curves of temperature, pore pressure and confining pressure. (a) Hydrate formation process and (b) triaxial shear process.

Fig. 9 shows the T_2 distribution, macropore peak shift and S_h change of hydrous quartz sand with $S_{w0} = 60.74\%$ and $\sigma_3 = 2.5$ MPa during hydrate formation. In Fig. 8(a), the T_2 spectrum at 0 min exhibits a bimodal distribution, with pore water predominantly occupying macropores. Over time, the macropore peak decreases significantly. Concurrently, S_h increases sharply and the macropore peak progressively shifts leftward (Fig. 8(b)), which is attributed to the decrease in pore size caused by the gradual filling of macropores by hydrates. However, the increase in the peak value of micropore at 0-16 min indicates that the rapid hydrate formation converts partial macropores into micropores, confirming that hydrate formation in micropores lags behind that in macropores (Pan et al., 2018; Cheng et al., 2021). Between 16-208 min, the decrease and leftward shift of the microporous peak indicate that hydrates begin to form in micropores. Between 208-1,623 min, the microporous peak continues to decline but exhibits a rightward shift, attributed to the lower ρ_2 of hydrates compared to quartz sand. Since hydrates tend to nucleate and grow on the surface of quartz sand, an increase in S_h will reduce the contact area of sand-water but enhance the contact area of hydrate-water, thereby enlarging the T_2 of microporous pore water. These findings align well with the law of CO_2 hydrate formation (Wang et al., 2024), confirming the high reliability and accuracy of the proposed experimental apparatus.

Fig. 10 displays the changes in pore water signal intensity and pore ratio during hydrate formation. Over time, the signal intensity of pore water in micropores first increases and then decreases, while that in macropores significantly decreases before gradually stabilizing. As S_h increases, the micropore ratio rises while the macropore ratio declines. The micropore peak becomes the new dominant peak at 1,623 min, consistent with previous findings (Handa and Stupin, 1992). Ultimately, some pore water fails to convert into hydrates under the effects of sediment surface property, capillary force and mass/heat transfer, and this phenomenon is more pronounced in micropores. Since hydrate formation reduces pore size and increases capillary forces, some pore water in micropores becomes less likely to form hydrates, hence the micropore ratio gradually increases.

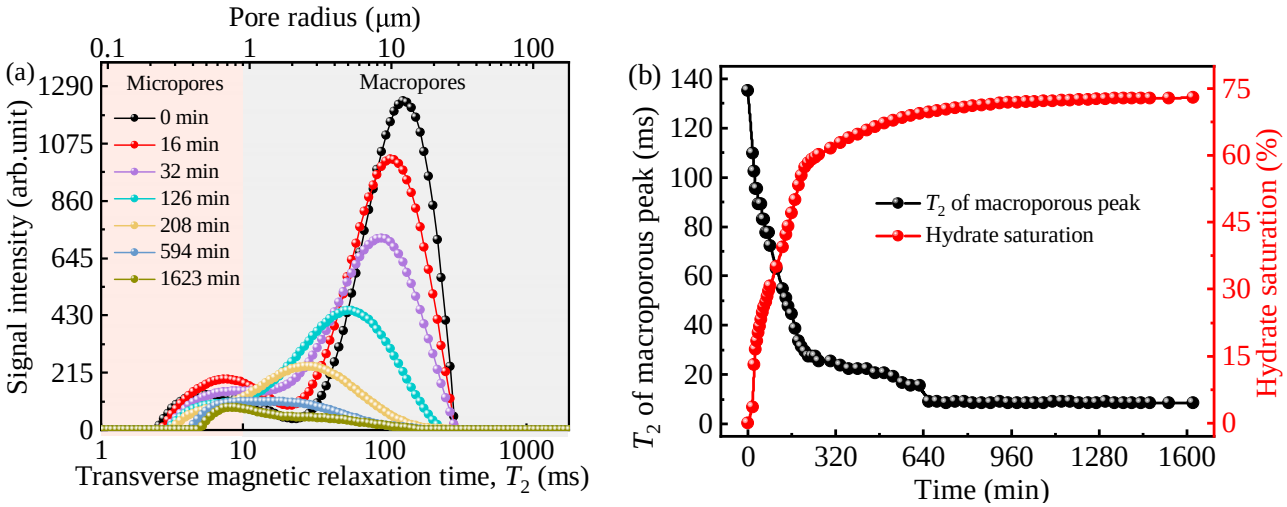

Fig. 9. $S_{w0} = 60.74\%$, $\sigma_3 = 2.5$ MPa system: (a) T_2 distribution and (b) macropore peak shift-S_h during hydrate formation.

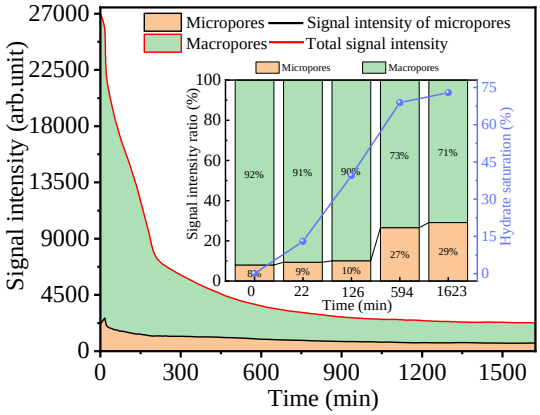

Fig. 10. In the $S_{w0} = 60.74\%$, $\sigma_3 = 2.5$ MPa system, the signal intensity, pore ratio and S_h changes during hydrate formation.

4.3 Correlation of NMR signal intensity and mechanical responses

In Fig. 11, the stress-strain curve, T_2 distribution, signal intensity, and pore ratio of the HBS system with $S_h = 57\%$, $\sigma_3 = 1.5$ MPa during shearing are displayed (see Fig. 11). As seen in Fig. 11(a), the stress-strain curve can be divided into three stages: elastic deformation stage under small strain (initial compaction stage), elastic-plastic deformation stage under moderate strain (plastic development stage), and strain-softening stage under large strain (plastic dilatation and crack development stage) (Miyazaki et al., 2011). Simultaneously, Fig. 11(b) shows the T_2 distributions measured at strains of 0, 5.1%, 10.04%, and 15.19%, corresponding to the four green points in Fig. 11(a). The ^{1}H signals in solids cannot be detected because the T_2 of ^{1}H in the solid phase is less than the echo spacing in the LF-NMR analyzer (Kleinberg, 2003). As the strain increases, the pore size distribution narrows and the signal intensity of the macroporous peak gradually increases (see Fig. 11(b)).

As shown in Figs. 11(b)-11(c), the cumulative signal intensity of micropores does not change obviously with the strain increasing, while that of macropores gradually increases. This indicates that water content in macropores is gradually increasing. Fig. 11(c) reveals that as strain increases, the total cumulative amplitude of T_2 distributions also increases. Besides, there is an increase of about 16.9% in the peak area of macropores with axial strain rising from 0 to 15%. As seen in Fig. 11(d), the proportion of micropores initially rises and then declines, while the macropore proportion first decreases and subsequently increases. At strains below 5.1%, the increase in micropore ratio and decrease in macropore ratio are primarily attributed to the insufficient compaction of sediment particles. Shear stress causes the macropore structure to be preferentially compressed, extruding some of the pore water, which is then redistributed into the surrounding micropores. This process increases the water saturation of the micropores, manifesting as an increase in micropore signal intensity. Furthermore, the macropores lacking filling and support are squeezed into micropores. When the strain exceeds 5.1%, the micropore proportion decreases while the macropore proportion increases with increasing strain. Concurrently, the stress increase slows down and the specimen undergoes dilatancy. This stems from the transition of sand particles from tight interlocking at the initial shear stage to friction, sliding and rotation, where the compression-hardening properties of the specimen are weakened but the shear stress continues to rise. Subsequently, the corners of some particles peel off and the released fragments fill the micropores, resulting in a decrease in the micropore ratio. Simultaneously, the high localized stress induces cementation failure at hydrate-sediment interfaces. With the development of cracks, both the signal intensity and ratio of macropores increase. The analysis of Fig. 11(a) demonstrates that when the strain exceeds 11.5%, the stress gradually declines from its peak.

4.4 CT-based verification of the results

The MRI image, binary MRI image and crack segmentation results from the X-CT scan images of the failed HBS specimen are shown in Fig. 12. The comparative analysis of post-shear

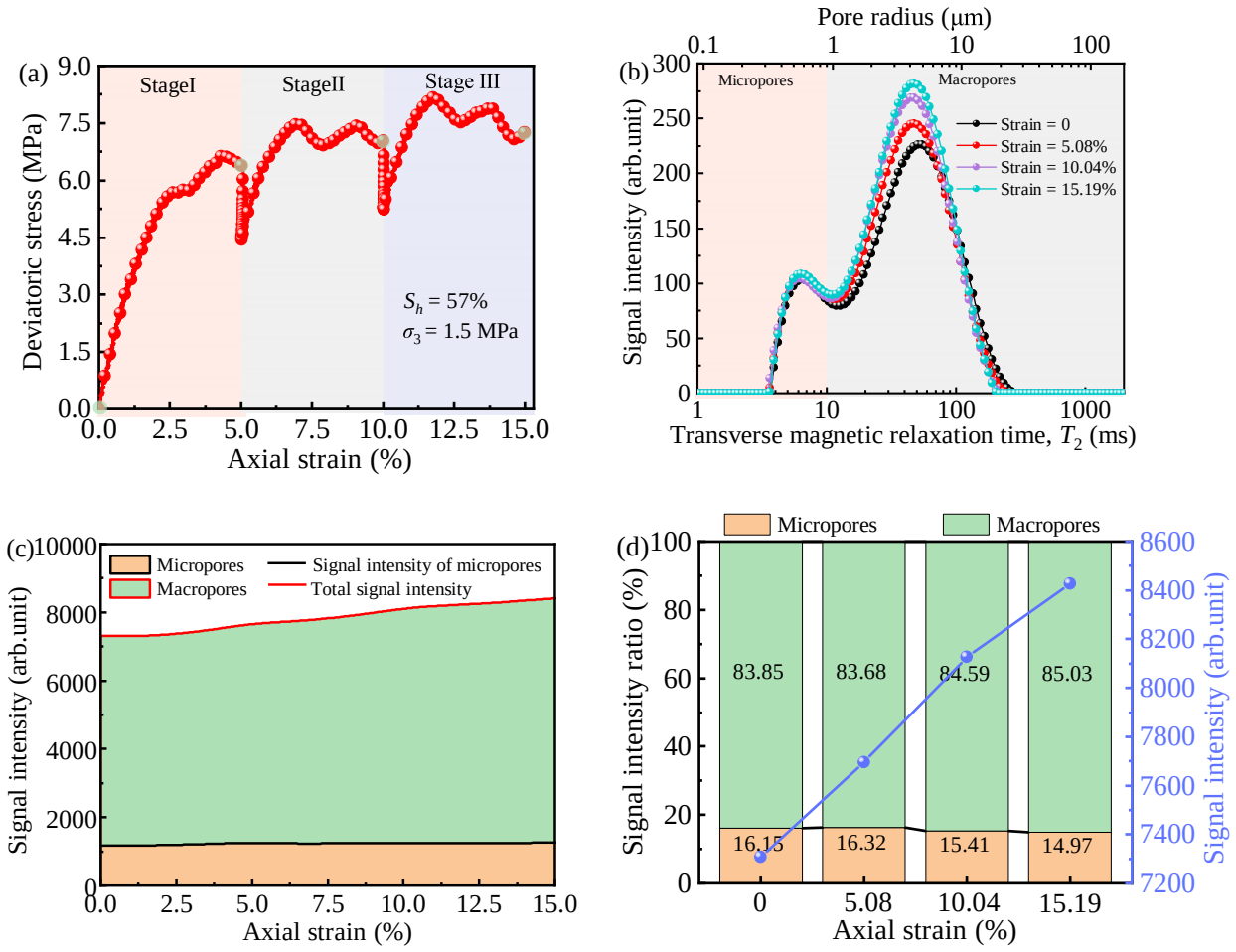

Fig. 11. (a) Stress-strain curve, (b) T_2 distribution, (c) signal intensities of micropores and macropores and (d) pore ratio and total signal intensity during shearing for the HBS specimen of $S_h = 57\%$, $\sigma_3 = 1.5$ MPa system.

specimen images, including MRI (Fig. 12(a)), binary image (Fig. 12(b)), and CT image (Fig. 12(c)), reveals that the position and morphology of Crack 1 and Crack 2 are highly consistent across the three types of images. This demonstrates that MRI technology can effectively track the evolution of microcracks during HBS shearing.

Cracks predominantly initiate at the specimen edges and propagate inward, and they do so with a certain inclination relative to the horizontal plane (see Figs. 12(a)-12(e)). During the shearing process, the pore-throat connectivity of the damaged region is obviously enhanced and cracks are formed (Fig. 12(c)-12(e)). Besides, the crack segmentation and 3D reconstruction results of X-CT images precisely locate the crack-damaged position of the specimen and realize the quantitative damage assessment of cracks. In this study, the location of the crack is regarded as the crack-damaged region. In Fig. 12(d), the specimen volume and crack volume are calculated as 14226.6 and 56.0822 mm^3, respectively. Therefore, the crack-damaged ratio is 0.3942%. The edges of specimens are more susceptible to damage due to the lack of support (Fig. 12(f)).

5. Conclusions

1) This study presents an integrated device for LF-NMR measurement and triaxial shear test of HBS, and the corresponding test methods are proposed. This technique can realize *in-situ* monitoring of the macro-mechanical response and micro-pore structure evolution of HBS specimens. The system consists of a high-pressure specimen vessel, an LF-NMR measurement module, a temperature-pressure control module, and a data acquisition module, and it integrates *in-situ* NGH synthesis, shear test, simultaneous acquisition of stress-strain curves, T_2 distribution, and MRI.
2) Preliminary experiments reveal that the technique can realize hydrate formation, which is in good agreement with previous research results, confirming that the device and test methods are highly reliable and applicable. With the strain rising from 0 to 15%, the peak area of macropores increases by 16.9%. During initial loading (strain $< 5\%$), the signal intensity ratio of micropores increases, while that of macropores decreases. However, the signal intensity ratio of both micropores and macropores presents an opposite trend with strain ranging from

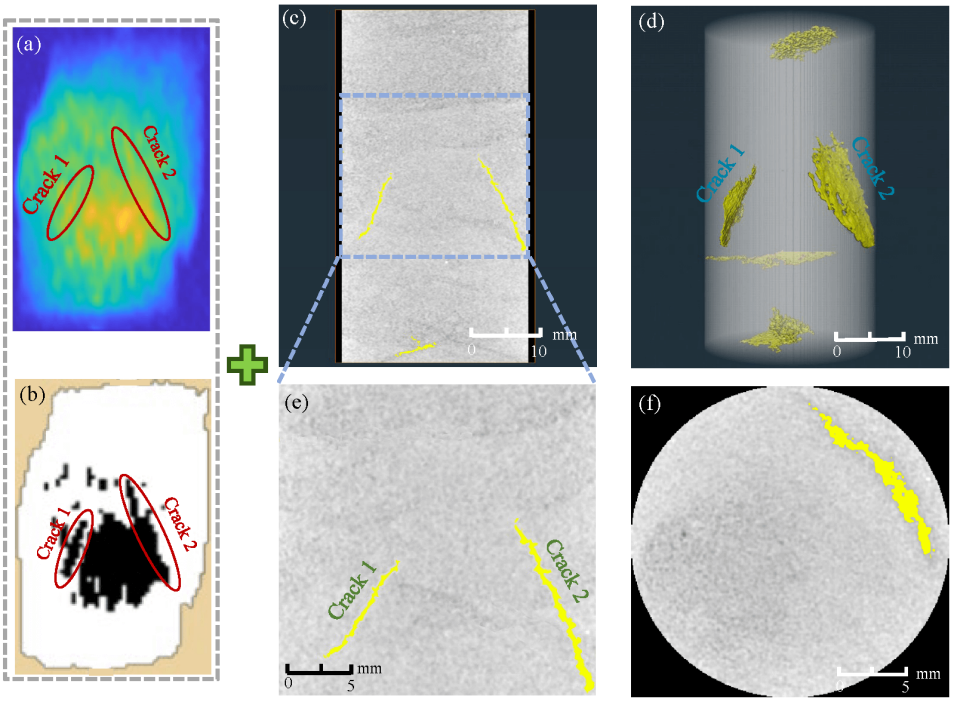

Fig. 12. MRI images and crack segmentation results from X-CT scan images. (a) MRI image, (b) binary MRI image, (c) side view of the specimen, (d) crack extraction and 3D reconstruction image, (e) local enlargement of cracks and (f) top view of the specimen.

5% to 15%. The positions and morphologies of cracks are highly consistent across the three types of images, verifying that MRI technology can effectively track the evolution of microcracks during HBS shearing.

3) This study implies the coupled evolution behaviors of mechanical response and pore structure in HBS. These breakthroughs establish a theoretical basis for the safe and efficient exploitation of NGH. Future research should focus on the micro- or macro-scale influencing factors that affect the correlations between LF-NMR signals and stress-strain curves. The technique may also apply to other geomaterials containing phase-reversible materials, such as frozen soil and salt-bearing strata.

Acknowledgements

This work was jointly supported by the National Key Research and Development Plan (No. 2023YFC2811001), the National Natural Science Foundation of China (Nos. U2444215, 42306242 and 42206231) and the Taishan Scholars Programs.

Conflict of interest

The authors declare no competing interest.

References

Bi, J., Ning, L., Zhao, Y., et al. Analysis of the microscopic evolution of rock damage based on real-time nuclear magnetic resonance. Rock Mechanics and Rock Engineering, 2023, 56(5): 3399-3411.

Bukhanov, B., Chuvilin, E., Mukhametdinova, A., et al. Estimation of residual pore water content in hydrate-bearing sediments at temperatures below and above 0 °C by NMR. Energy & Fuels, 2022, 36(24): 14789-14801.

Cheng, Z., Wang, S., Xu, N., et al. Quantitative analysis of methane hydrate formation in size-varied porous media for gas storage and transportation application. Fuel, 2021, 301: 121021.

Dong, L., Liu, X., Gong, B., et al. Geomechanical properties of hydrate-bearing strata and their applications. Advances in Geo-Energy Research, 2024, 11(3): 161-167.

Ersland, G., Husebø, J., Graue, A., et al. Measuring gas hydrate formation and exchange with CO_2 in Bentheim sandstone using MRI tomography. Chemical Engineering Journal, 2010, 158(1): 25-31.

Handa, Y. P., Stupin, D. Y. Thermodynamic properties and dissociation characteristics of methane and propane hydrates in 70-.ANG.-radius silica gel pores. The Journal of Physical Chemistry, 1992, 96(21): 8599-8603.

Hyodo, M., Li, Y. H., Yoneda, J., et al. Mechanical behavior of gas-saturated methane hydrate-bearing sediments. Journal of Geophysical Research: Solid Earth, 2013, 118(10): 5185-5194.

Hyodo, M., Wu, Y., Nakashima, K., et al. Influence of fines content on the mechanical behavior of methane hydrate-

bearing sediments. Journal of Geophysical Research: Solid Earth, 2017, 122(10): 7511-7524.

Ji, Y., Liu, C., Zhang, Z., et al. Experimental study on characteristics of pore water conversion during methane hydrates formation in unsaturated sand. China Geology, 2022, 5(2): 276-284.

Kleinberg, R. L. Seafloor nuclear magnetic resonance assay of methane hydrate in sediment and rock. Journal of Geophysical Research: Solid Earth, 2003, 108(B3): 2137.

Kossel, E., Deusner, C., Bigalke, N., et al. The dependence of water permeability in quartz sand on gas hydrate saturation in the pore space. Journal of Geophysical Research: Solid Earth, 2018, 123(2): 1235-1251.

Li, Y., Dong, L., Wu, N., et al. Influences of hydrate layered distribution patterns on triaxial shearing characteristics of hydrate-bearing sediments. Engineering Geology, 2021b, 294: 106375.

Li, Y., Liu, L., Jin, Y., et al. Characterization and development of natural gas hydrate in marine clayey-silt reservoirs: A review and discussion. Advances in Geo-Energy Research, 2021a, 5(1): 75-86.

Liu, L., Zhang, Z., Liu, C., et al. Nuclear magnetic resonance transverse surface relaxivity in quartzitic sands containing gas hydrate. Energy & Fuels, 2021, 35(7): 6144-6152.

Makogon, Y. F., Holditch, S. A., Makogon, T. Y. Natural gas-hydrates – a potential energy source for the 21st century. Journal of Petroleum Science and Engineering, 2007, 56(1): 14-31.

Minagawa, H., Egawa, K., Sakamoto, Y., et al. Characterization of hydraulic permeability of methane-hydrate-bearing sediment estimated by T_2-distribution of proton NMR. Paper ISOPE-I-12-041 Presented at the Twenty-second International Offshore and Polar Engineering Conference, Rhodes, Greece, 17-22 June, 2012.

Miyazaki, K., Masui, A., Sakamoto, Y., et al. Triaxial compressive properties of artificial methane-hydrate-bearing sediment. Journal of Geophysical Research: Solid Earth, 2011, 116(B6): B06102.

Miyazaki, K., Tenma, N., Sakamoto, Y., et al. Effects of methane hydrate saturation and confining pressure on strain-rate dependence of artificial methane-hydrate-bearing sediment in triaxial compression test. International Journal of Offshore and Polar Engineering, 2012, 22(1): 90-96.

Pan, Z., Liu, Z., Zhang, Z., et al. Effect of silica sand size and saturation on methane hydrate formation in the presence of SDS. Journal of Natural Gas Science and Engineering, 2018, 56: 266-280.

Shumskayte, M. Y., Manakov, A. Y., Sagidullin, A. K., et al. Melting of tetrahydrofuran hydrate in pores: An investigation by low-field NMR relaxation. Marine and Petroleum Geology, 2021, 129: 105096.

Slijkerman, W. F., Hofman, J. P., Looyestijn, W. J., et al. A Practical approach to obtain primary drainage capillary pressure curves from NMR core and log data. Petrophysics, 2001, 42(4): 334-343.

Sloan, E. D. Fundamental principles and applications of natural gas hydrates. Nature, 2003, 426(6964): 353-359.

Sloan, J., Dandy, E., Koh, C. A. 2008. Clathrate Hydrates of Natural Gases, Boca Raton, USA, CRC Press, 2007.

Sohn, Y., Park, T., Kwon, T. H. Geomechanical responses of sand-clay interbedded gas hydrate-bearing deposits under depressurization-driven gas production at site UBGH2-6 in Ulleung Basin, offshore Korea. Gas Science and Engineering, 2024, 126: 205337.

Walsh, M. R., Koh, C. A., Sloan, E. D., et al. Microsecond Simulations of Spontaneous Methane Hydrate Nucleation and Growth. Science, 2009, 326(5956): 1095-1098.

Wang, J., Ji, Y., Liu, C., et al. Dependence of the hydrate-based CO_2 storage characteristics on sand particle size and clay content in unconsolidated sediments. Chemical Engineering Journal, 2024, 501: 157497.

Wu, Z., Li, Y., Sun, X., et al. Experimental study on the gas phase permeability of montmorillonite sediments in the presence of hydrates. Marine and Petroleum Geology, 2018, 91: 373-380.

Yao, Y., Liu, D., Che, Y., et al. Petrophysical characterization of coals by low-field nuclear magnetic resonance (NMR). Fuel, 2010, 89(7): 1371-1380.

Yoneda, J., Takiguchi, A., Ishibashi, T., et al. Mechanical response of reservoir and well completion of the first offshore methane-hydrate production test at the eastern Nankai trough: a coupled thermo-hydromechanical analysis. SPE Journal, 2019, 24(2): 531-546.

Zhang, Y., Li, Y., Chen, M., et al. Experimental study on direct shear properties and shear surface morphologies of hydrate-bearing sediments. Gas Science and Engineering, 2024a, 128: 205387.

Zhang, Y., Li, Y., Wu, N., et al. Integrated test system for interfacial strength and morphology of multi-type hydrate-bearing sediments. Review of Scientific Instruments, 2024b, 95(9): 095101.

Zhao, Y., Wang, C., Ning, L., et al. Pore and fracture development in coal under stress conditions based on nuclear magnetic resonance and fractal theory. Fuel, 2022, 309: 122112.

Zhou, H., Liu, Z., Zhong, J., et al. NMRI online observation of coal fracture and pore structure evolution under confining pressure and axial compressive loads: A novel approach. Energy, 2022, 261: 125297.